Supporting Information

Frustrated Lewis pair adducts of alkynyl-capped tetrelenes

Abhishek V. Muralidharan,[a] Brandon L. Frenette,[a] Julius Wicke,[b] Alvaro A. Omaña,[a] Michael J. Ferguson,[a] and Eric Rivard*[,a]

[a] *Department of Chemistry, University of Alberta, 11227 Saskatchewan Drive, Edmonton, Alberta, Canada T6G 2G2*

[b] *Institut für Anorganische und Analytische Chemie, Goethe-Universität Frankfurt, Max-von-Laue-Straße 7, D-60438, Frankfurt am Main, Germany*

Table of Contents

1. NMR spectra

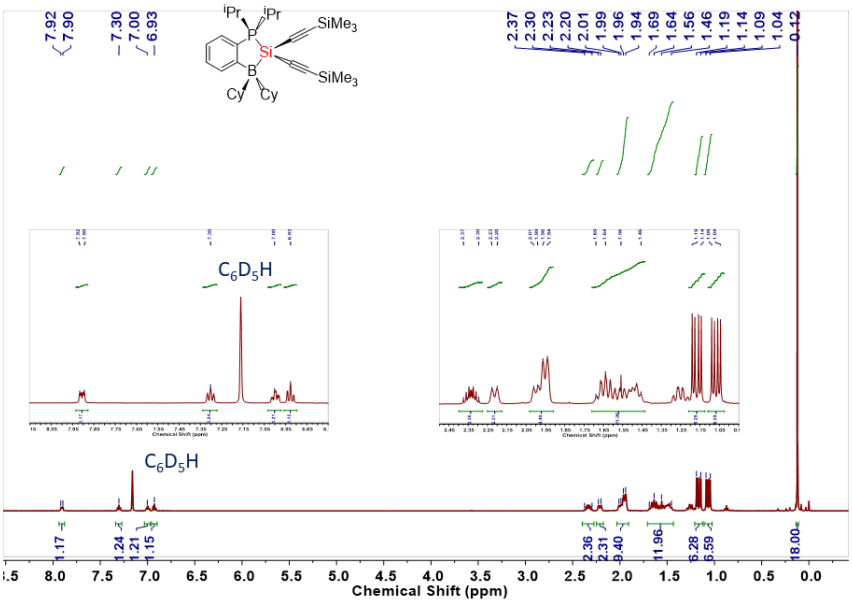

Fig. S1. ^{1}H NMR spectrum of PB{Si(C≡CSiMe$_3$)$_2$} (**3**) in C_6D_6.

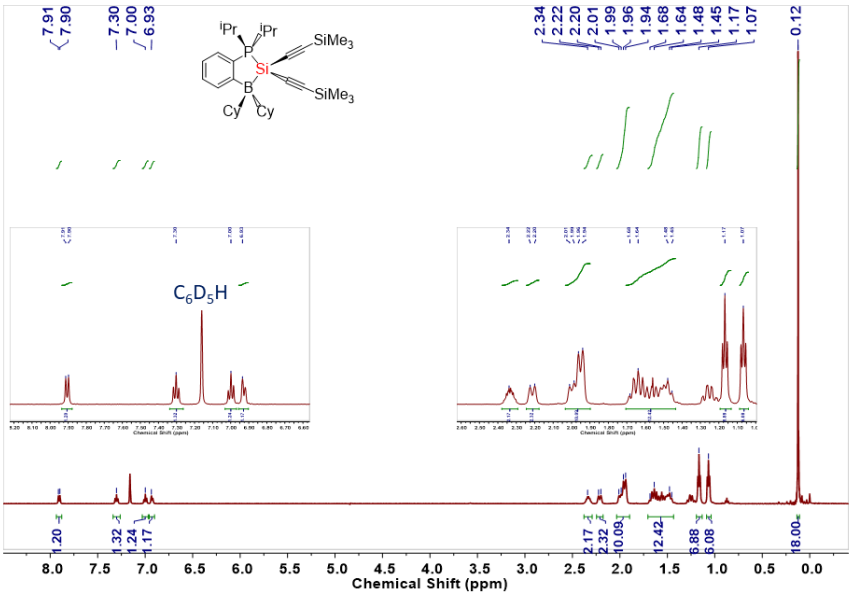

Fig. S2. $^{1}H\{^{31}P\}$ NMR spectrum of PB{Si(C≡CSiMe$_3$)$_2$} (**3**) in C_6D_6.

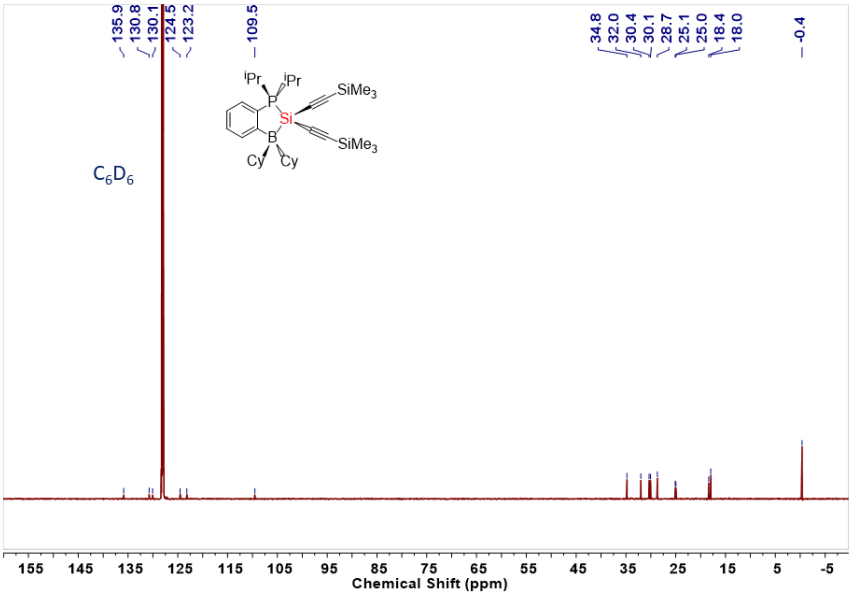

Fig. S3. $^{13}C\{^{1}H\}$ NMR spectrum of PB{Si(C≡CSiMe$_3$)$_2$} (**3**) in C_6D_6.

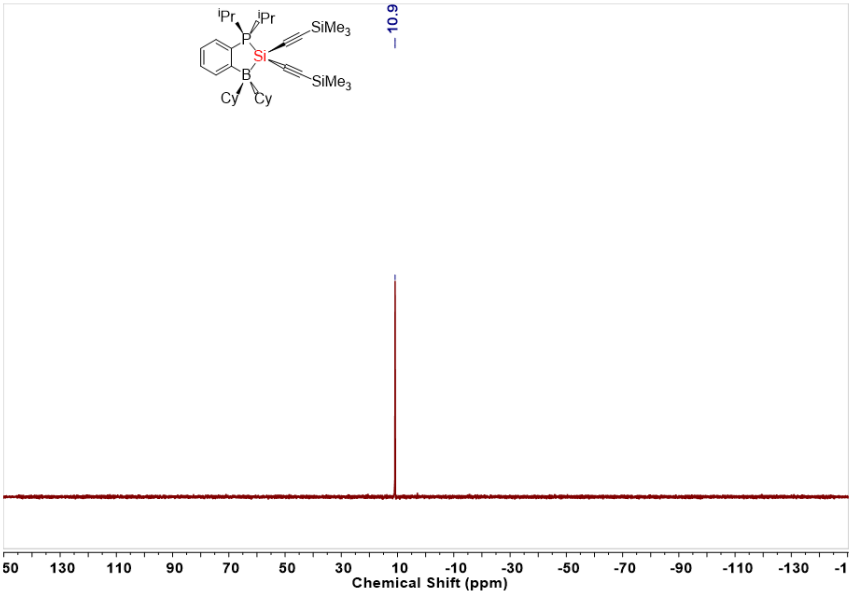

Fig. S4. $^{31}P\{^{1}H\}$ NMR spectrum of PB{Si(C≡CSiMe$_3$)$_2$} (**3**) in C_6D_6.

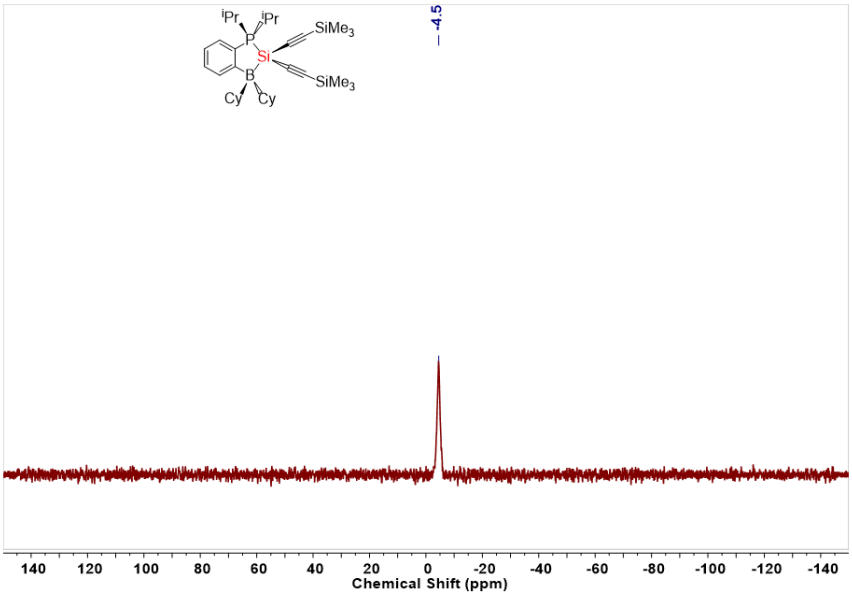

Fig. S5. $^{11}B\{^{1}H\}$ NMR spectrum of PB{Si(C≡CSiMe$_3$)$_2$} (**3**) in C_6D_6.

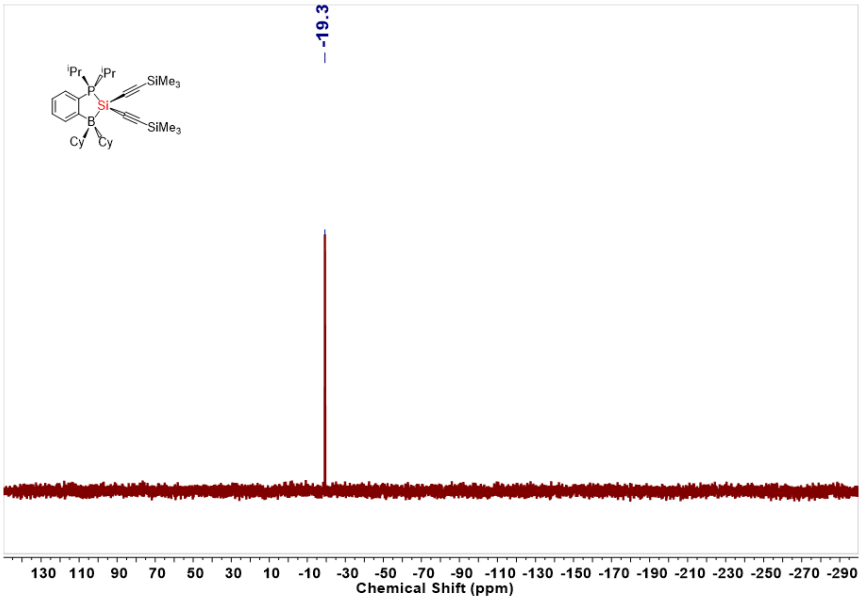

Fig. S6. $^{29}Si\{^{1}H\}$ (DEPT) NMR spectrum of PB{Si(C≡CSiMe$_3$)$_2$} (**3**) in C_6D_6.

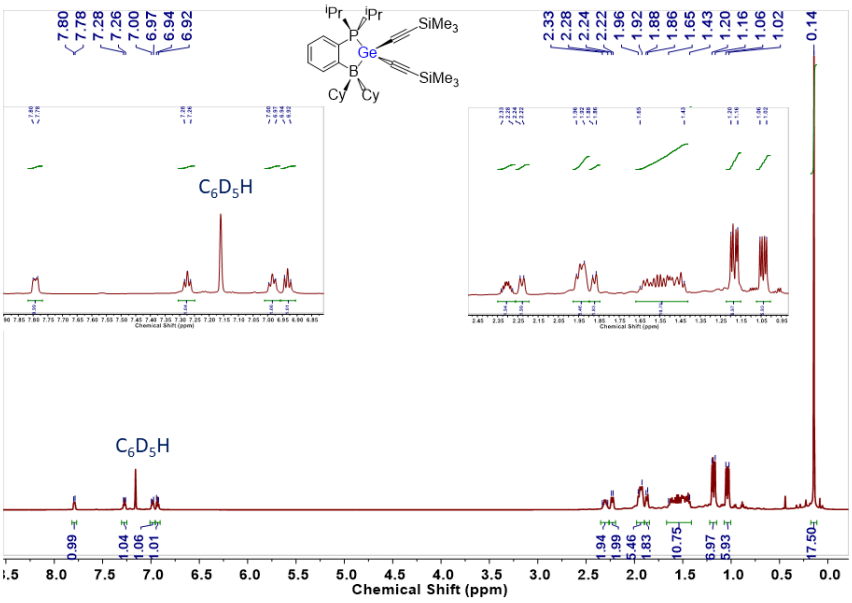

Fig. S7. ^{1}H NMR spectrum of PB{Ge(C≡CSiMe$_3$)$_2$} (**4**) in C_6D_6.

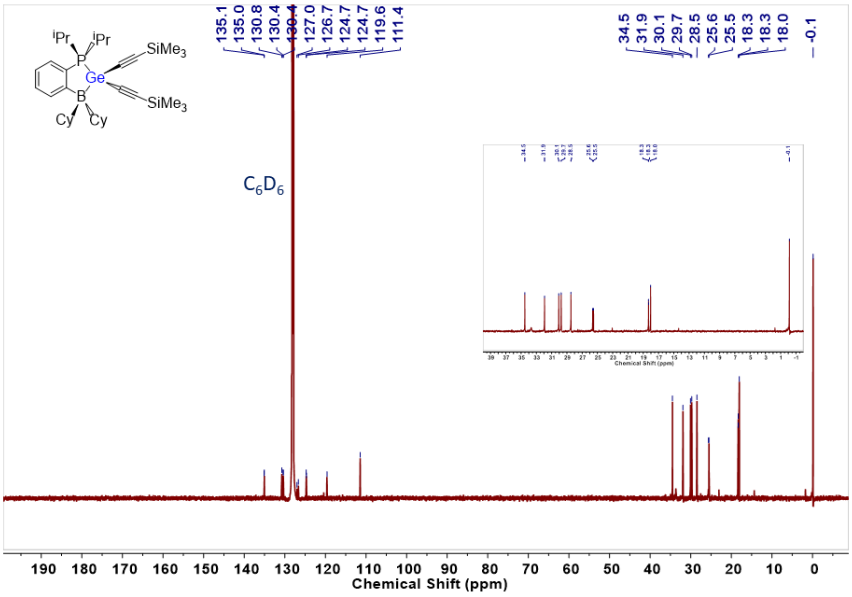

Fig. S8. $^{13}C\{^1H\}$ NMR spectrum of PB{Ge(C≡CSiMe$_3$)$_2$} (**4**) in C_6D_6.

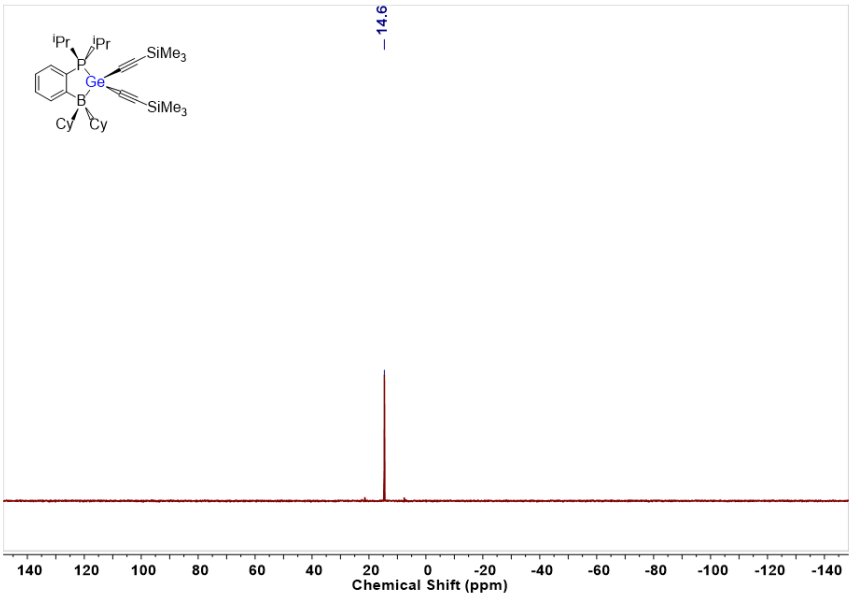

Fig. S9. $^{31}P\{^1H\}$ NMR spectrum of PB{Ge(C≡CSiMe$_3$)$_2$} (**4**) in C_6D_6.

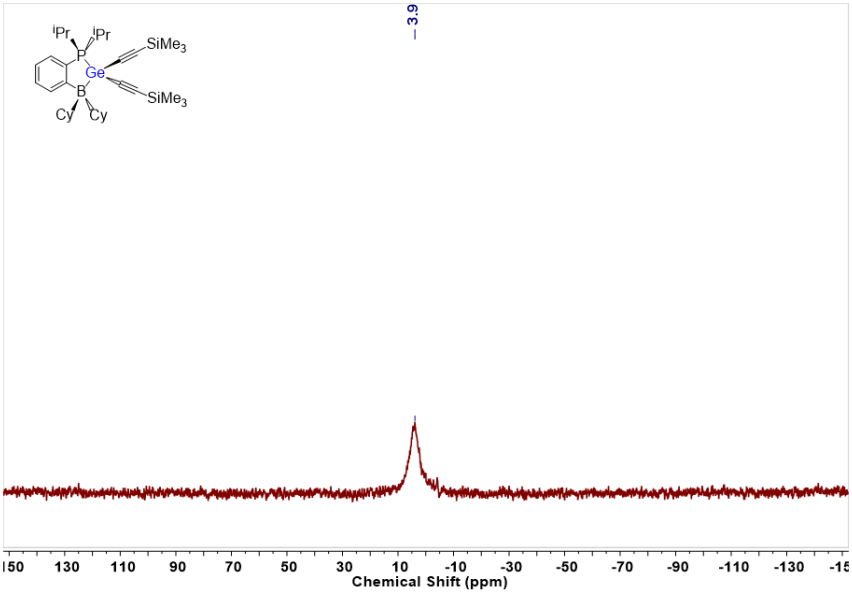

Fig. S10. $^{11}B\{^{1}H\}$ NMR spectrum of $PB\{Ge(C{\equiv}CSiMe_3)_2\}$ (**4**) in C_6D_6.

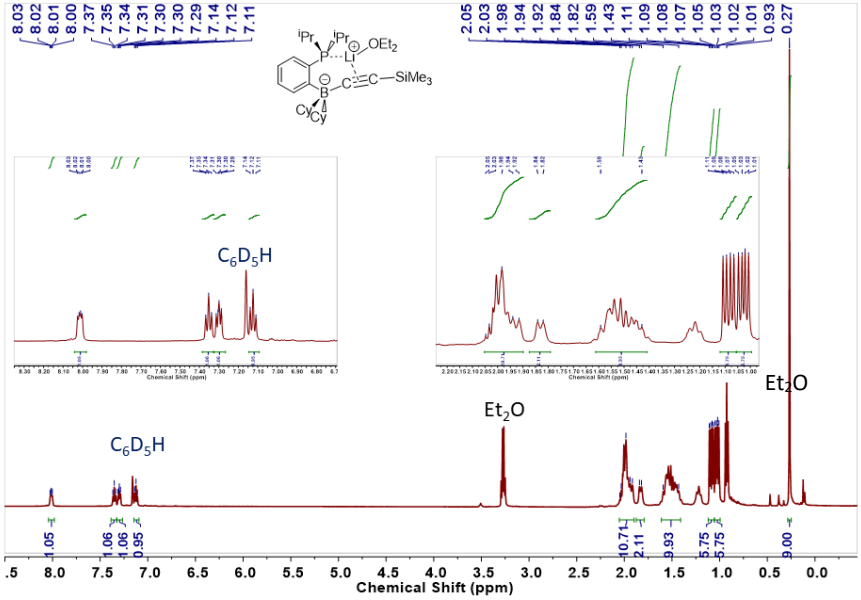

Fig. S11. ^{1}H NMR spectrum of $[PB\{C{\equiv}CSiMe_3\}Li(OEt_2)]$ (**5**) in C_6D_6.

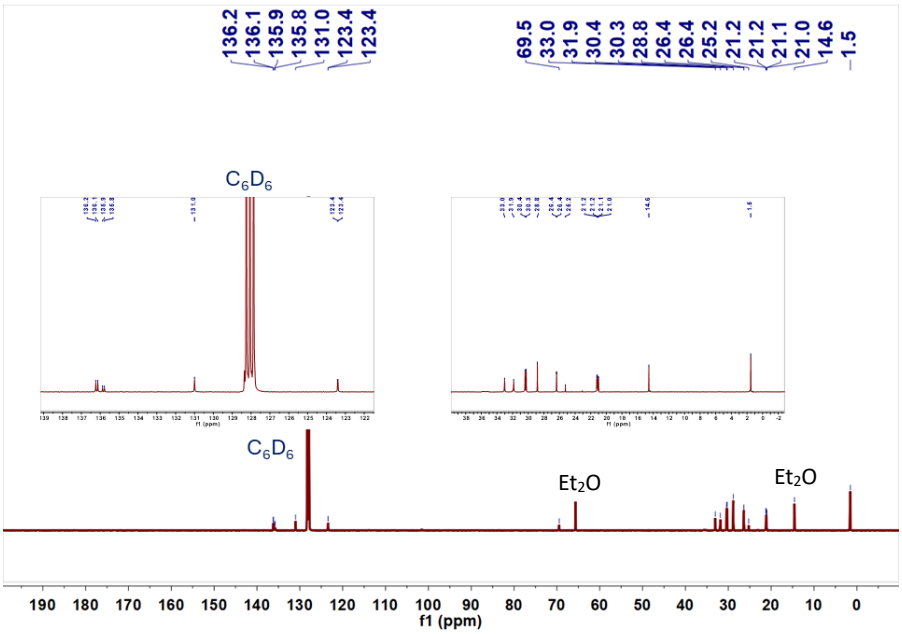

Fig. S12. $^{13}C\{^{1}H\}$ NMR spectrum of [PB{C≡CSiMe$_3$}Li(OEt$_2$)] (**5**) in C_6D_6.

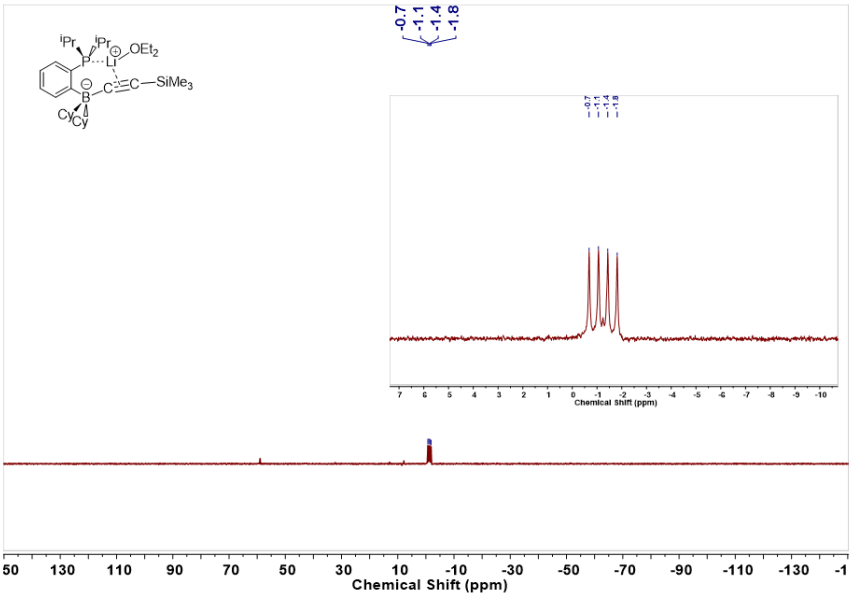

Fig. S13. $^{31}P\{^{1}H\}$ NMR spectrum of [PB{C≡CSiMe$_3$}Li(OEt$_2$)] (**5**) in C_6D_6.

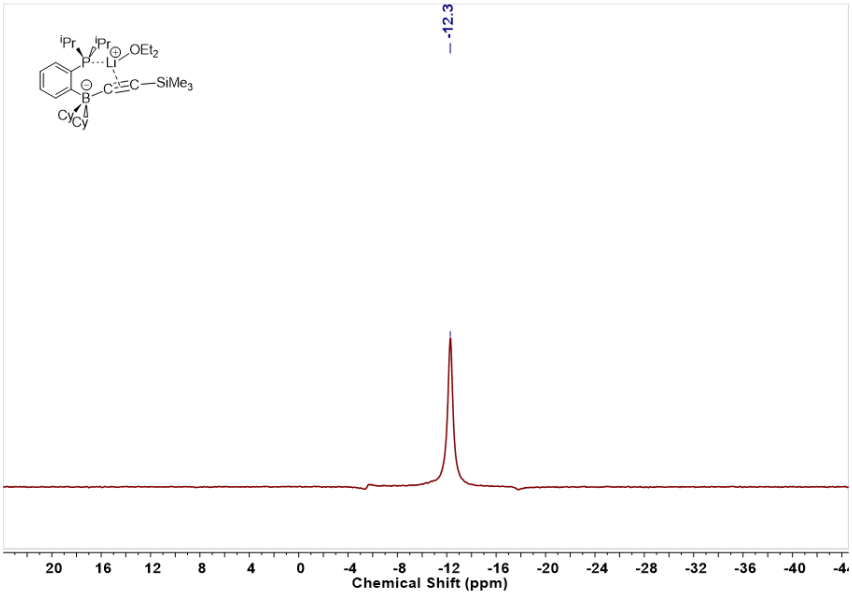

Fig. S14. $^{11}B\{^{1}H\}$ NMR spectrum of [PB{C≡CSiMe$_3$}Li(OEt$_2$)] (**5**) in C_6D_6.

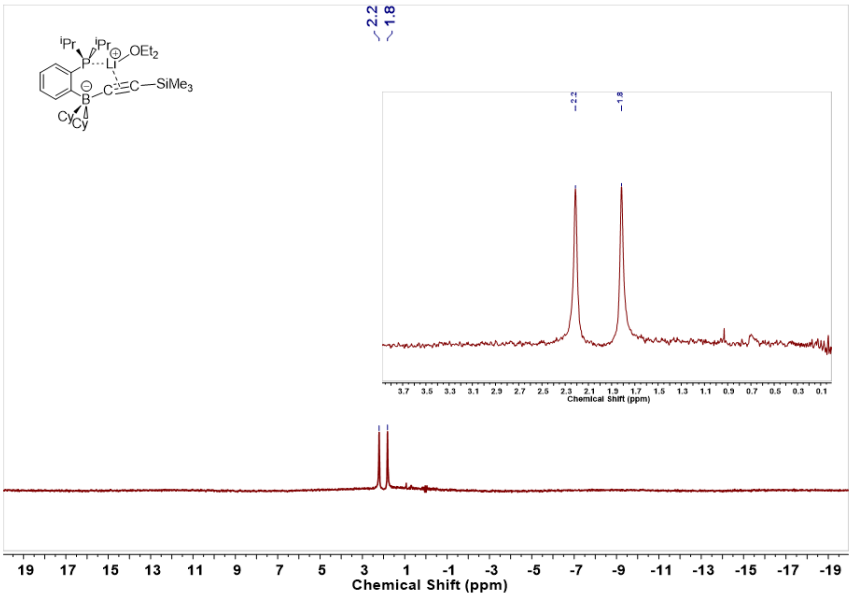

Fig. S15. $^{7}Li\{^{1}H\}$ NMR spectrum of [PB{C≡CSiMe$_3$}Li(OEt$_2$)] (**5**) in C_6D_6.

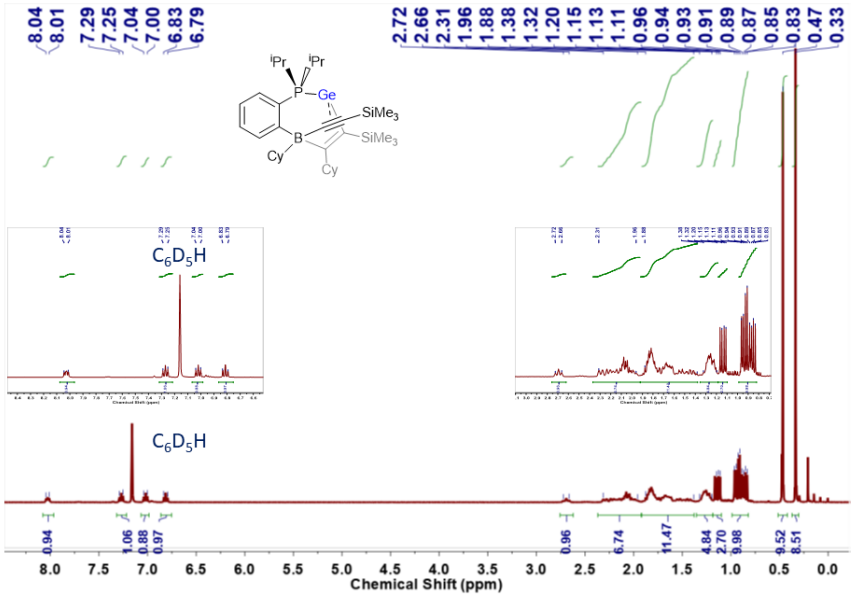

Fig. S16. ^{1}H NMR spectrum of **6** in C_6D_6.

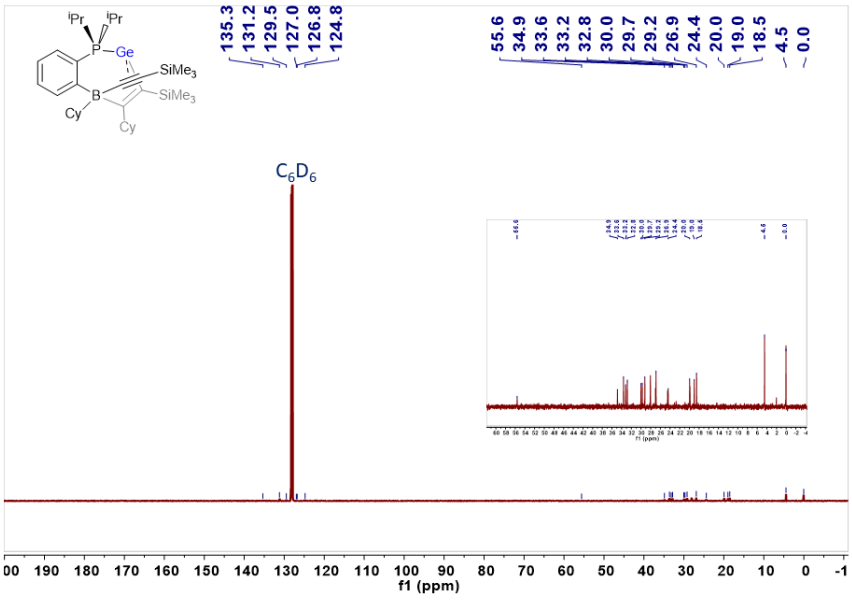

Figure S17. $^{13}C\{^{1}H\}$ NMR spectrum of **6** in C_6D_6.

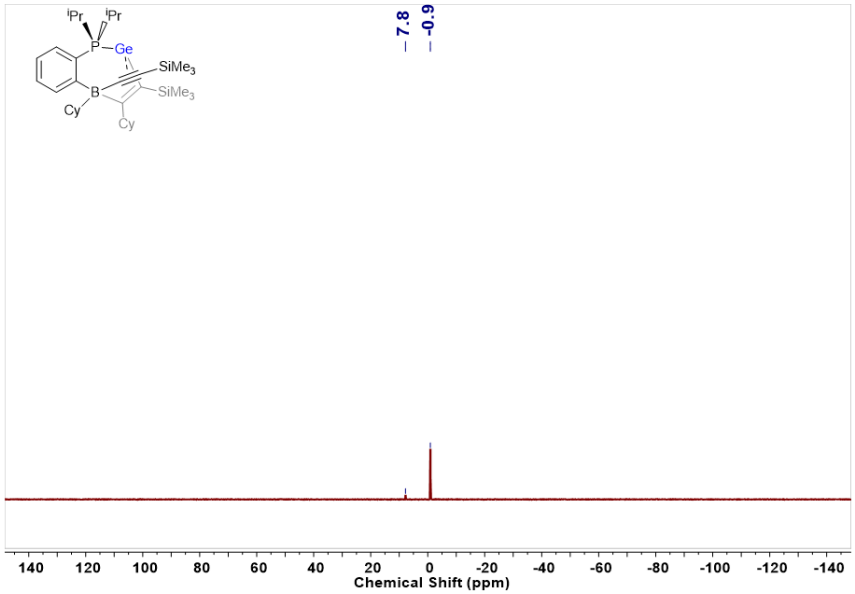

Figure S18. $^{31}P\{^{1}H\}$ NMR spectrum of **6** in C_6D_6.

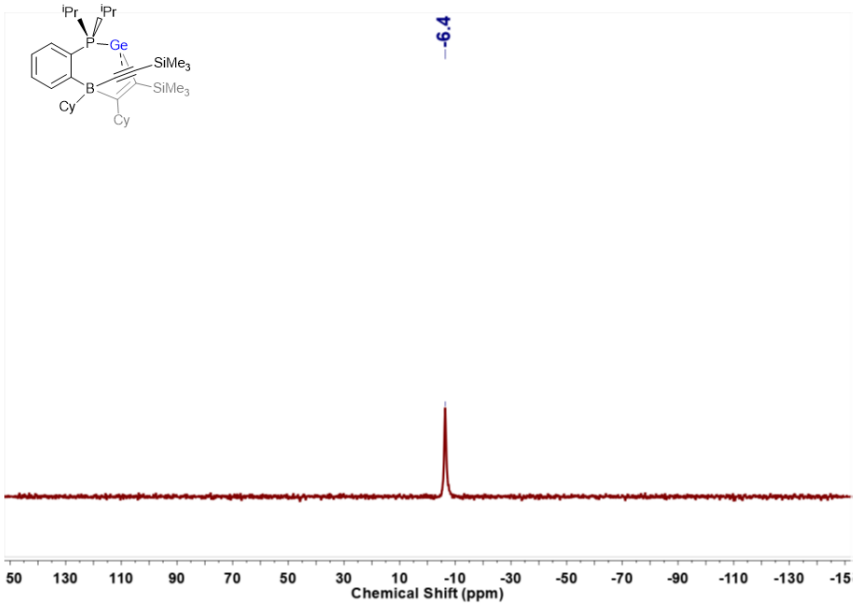

Figure S19. $^{11}B\{^{1}H\}$ NMR spectrum of **6** in C_6D_6.

2. X-ray crystallography

Appropriate X-ray quality crystals were coated with a small amount of hydrocarbon oil (Paratone-N) and removed from the glovebox in a vial. A crystal was then selected, quickly mounted on a loop, and placed in a low temperature stream of nitrogen on the X-ray diffractometer. All data were collected using a Bruker APEX II CCD detector on a D8 Duo or PLATFORM diffractometer using Mo Kα (0.71073 Å) or Cu Kα (1.54178 Å) radiation.

The data was corrected for absorption through Gaussian integration from the indexing of crystal faces. [S1] Crystal structures were solved via intrinsic phasing (SHELXT) and refined using SHELXL,[S2] using Olex2 as a GUI.[S3] The assignment of carbon-bound hydrogen atom positions are based on the sp^2 - or sp^3 - hybridization geometries of their attached carbon atoms and were given thermal parameters 20 % greater than those of their parent atoms. Hydrogen atoms bound to heteroatoms were located in the difference Fourier maps and refined isotropically. Molecular structures are shown with thermal ellipsoids at a 50 % probability level and have been imaged using Diamond.[S4] All crystal structures were deposited into the Cambridge Crystallographic Data Centre (CCDC) database with accession numbers 2337934-2337936.

Note: The quality of the crystal data for **6** is insufficient to deposit into the Cambridge Crystallographic Data Centre (CCDC) database; the .CIF file will be available upon request from the author.

Table S1. X-ray crystallographic data for PB{Si(C≡CSiMe$_3$)$_2$} (**3**).

Empirical formula	$C_{34}H_{58}BPSi_3$
Formula weight	592.85
Temperature/K	193.15
Crystal system	monoclinic
Space group	$P2_1/n$
a/Å	11.7526(12)
b/Å	19.307(2)
c/Å	16.8909(17)
α/°	90
β/°	105.0956(17)
γ/°	90
Volume/Å^3	3700.5(7)
Z	4
ρ_{calc} g/cm^3	1.064
μ/mm^{-1}	0.192
F(000)	1296.0
Crystal size/mm^3	0.469 × 0.372 × 0.14
Radiation	MoKα (λ = 0.71073)
2Θ range for data collection/°	3.27 to 56.658
Index ranges	-15 ≤ h ≤ 15, -25 ≤ k ≤ 25, -22 ≤ l ≤ 22
Reflections collected	86565
Independent reflections	9233 [R_{int} = 0.0510, R_{sigma} = 0.0254]
Data/restraints/parameters	9233/3/378
Goodness-of-fit on F^2	1.037
Final R indexes [I>=2σ (I)][a]	R_1 = 0.0433, wR_2 = 0.1149
Final R indexes [all data][a]	R_1 = 0.0556, wR_2 = 0.1260
Largest diff. peak/hole / e Å^{-3}	0.33/-0.31

[a] $R1 = \Sigma||Fo| - |Fc||/\Sigma|Fo|$; $wR2 = [\Sigma w(Fo^2 - Fc^2)^2/\Sigma w(Fo^4)]^{1/2}$

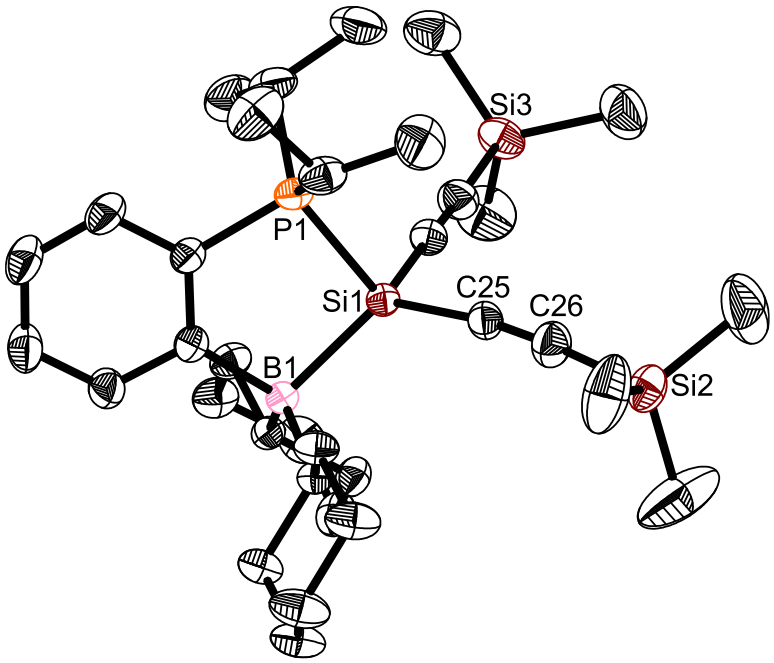

Fig. S20. Molecular structure of PB{Si(C≡CSiMe$_3$)$_2$} (**3**) with thermal ellipsoids plotted at 50 %. Only the major component [86.6(4) %] of the disordered trimethylsilyl group is shown, and all H atoms are omitted for clarity. Selected bond lengths [Å] and angles [°]: P1–Si1 2.3050(6), B1–Si1 2.0706(16), Si1–C25 1.8451(15), Si1–C30 1.8520(15), C25–C26 1.202(2), C30-C31 1.197(2); Si1–C25–C26 171.97(15), S1-C30-C31 177.67(15).

Table S2. X-ray crystallographic data for PB{Ge(C≡CSiMe$_3$)$_2$} (**4**).

Empirical formula	$C_{34}H_{58}BGePSi_2$
Formula weight	637.35
Temperature/K	193.15
Crystal system	monoclinic
Space group	$P2_1/n$
a/Å	11.9583(15)
b/Å	20.414(3)
c/Å	16.094(2)
α/°	90
β/°	107.665(2)
γ/°	90
Volume/Å^3	3743.7(8)
Z	4
ρ_{calc}g/cm^3	1.131
μ/mm^{-1}	0.945
F(000)	1368.0
Crystal size/mm^3	0.516 × 0.048 × 0.043
Radiation	MoKα (λ = 0.71073)
2θ range for data collection/°	3.322 to 52.97
Index ranges	-14 ≤ h ≤ 14, -25 ≤ k ≤ 25, -20 ≤ l ≤ 20
Reflections collected	44085
Independent reflections	7726 [R_{int} = 0.0906, R_{sigma} = 0.0664]
Data/restraints/parameters	7726/0/362
Goodness-of-fit on F^2	1.022
Final R indexes [I>=2σ (I)][a]	R_1 = 0.0446, wR_2 = 0.0962
Final R indexes [all data][a]	R_1 = 0.0773, wR_2 = 0.1118
Largest diff. peak/hole / e Å^{-3}	0.70/-0.29

[a]$R1 = \Sigma||Fo| - |Fc||/\Sigma|Fo|$; $wR2 = [\Sigma w(Fo^2 - Fc^2)^2/\Sigma w(Fo^4)]^{1/2}$

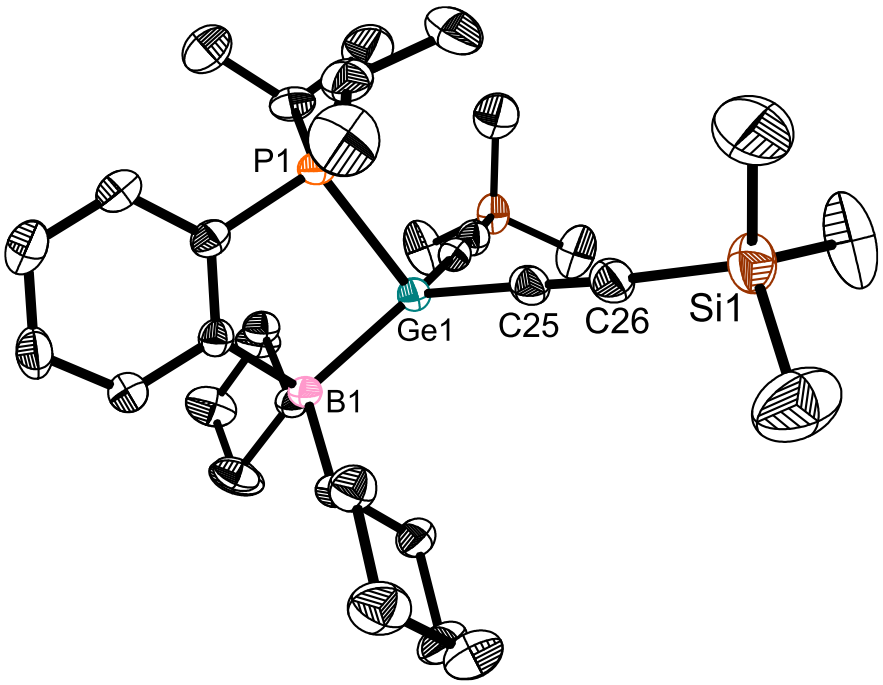

Fig. S21. Molecular structure of PB{Ge(C≡CSiMe$_3$)$_2$} (**4**) with thermal ellipsoids plotted at 50 %. Selected bond lengths [Å] and angles [°]: Ge1–P1 2.3695(8), Ge1–C25 1.928(3), Ge1–B1 2.157(3), Ge1–C30 1.926(3), C25–C26 1.205(4), C30–C31 1.207(4); C26–C25–Ge1 178.9(3), C31–C30–Ge1 175.1(3).

Table S3. X-ray crystallographic data for [PB{C≡CSiMe$_3$}Li(OEt$_2$)] (**5**).

Empirical formula	$C_{33}H_{59}BLiOPSi$
Formula weight	548.61
Temperature/K	193.15
Crystal system	monoclinic
Space group	$P2_1/n$
a/Å	9.528(2)
b/Å	20.445(5)
c/Å	17.796(5)
α/°	90
β/°	98.843(3)
γ/°	90
Volume/Å^3	3425.2(15)
Z	4
ρ_{calc}g/cm^3	1.064
μ/mm^{-1}	0.138
F(000)	1208.0
Crystal size/mm^3	0.258 × 0.198 × 0.05
Radiation	MoKα (λ = 0.71073)
2Θ range for data collection/°	3.054 to 50.802
Index ranges	-11 ≤ h ≤ 11, -24 ≤ k ≤ 24, -21 ≤ l ≤ 21
Reflections collected	6303
Independent reflections	6303 [R_{int} = 0.1474, R_{sigma} = 0.0762]
Data/restraints/parameters	6303/42/363
Goodness-of-fit on F^2	1.057
Final R indexes [I>=2σ (I)][a]	R_1 = 0.0875, wR_2 = 0.2223
Final R indexes [all data][a]	R_1 = 0.1458, wR_2 = 0.2583
Largest diff. peak/hole / e Å^{-3}	0.68/-0.46

[a]$R1 = \Sigma||Fo| - |Fc||/\Sigma|Fo|$; $wR2 = [\Sigma w(Fo^2 - Fc^2)^2/\Sigma w(Fo^4)]^{1/2}$

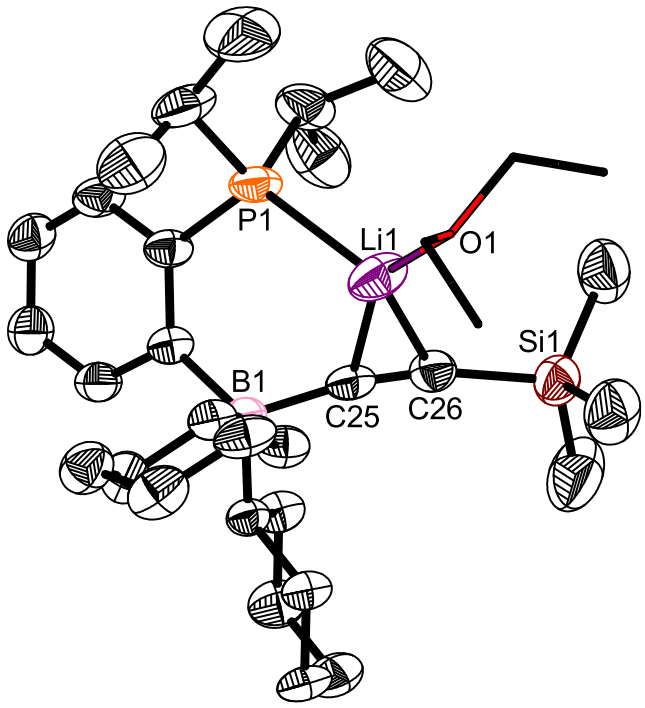

Fig. S22. Molecular structure of [PB{C≡CSiMe$_3$}Li(OEt$_2$)] (**5**) with thermal ellipsoids plotted at 50 %. Only the major [89.7(7) %] component of the disordered Cy ring is shown, and the coordinated ether molecule is shown in wireframe. All H atoms are omitted for clarity. Selected bond lengths [Å] and angles [°]: P1–Li1 2.492(7), C25–B1 1.622(6), C25–Li1 2.226(8), C26–Li1 2.261(9), C25–C26 1.205(5); C26–C25–B1 170.2(4), C25–C26–Si1 166.6(4), C25–Li1–P1 86.1(3).

Table S4. X-ray crystallographic data for **6**.

Empirical formula	$C_{34}H_{58}BGePSi_2$
Formula weight	637.35
Temperature/K	173
Crystal system	monoclinic
Space group	$P2_1/c$
a/Å	19.6008(12)
b/Å	20.4499(13)
c/Å	19.6146(12)
α/°	90
β/°	11.430(4)
γ/°	90
Volume/Å^3	7213.9(8)
Z	8
ρ_{calc}g/cm^3	1.174
μ/mm^{-1}	2.345
F(000)	2736.0
Crystal size/mm^3	0.376 × 0.042 × 0.015
Radiation	Cu Kα (1.54178 Å)
2θ range for data collection/°	4.914 to 135.378
Index ranges	-23 ≤ h ≤ 23, -24 ≤ k ≤ 24, -23 ≤ l ≤ 23
Reflections collected	172572
Independent reflections	13056 [R_{int} = 0.1725, R_{sigma} = 0.0643]
Data/restraints/parameters	13056/30/755
Goodness-of-fit on F^2	1.405
Final R indexes [I>=2σ (I)][a]	R_1 = 0.1303, wR_2 = 0.3696
Final R indexes [all data][a]	R_1 = 0.1664, wR_2 = 0.4019
Largest diff. peak/hole / e Å^{-3}	1.93/-1.45

[a]$R1 = \Sigma||Fo| - |Fc||/\Sigma|Fo|$; $wR2 = [\Sigma w(Fo^2 - Fc^2)^2/\Sigma w(Fo^4)]^{1/2}$

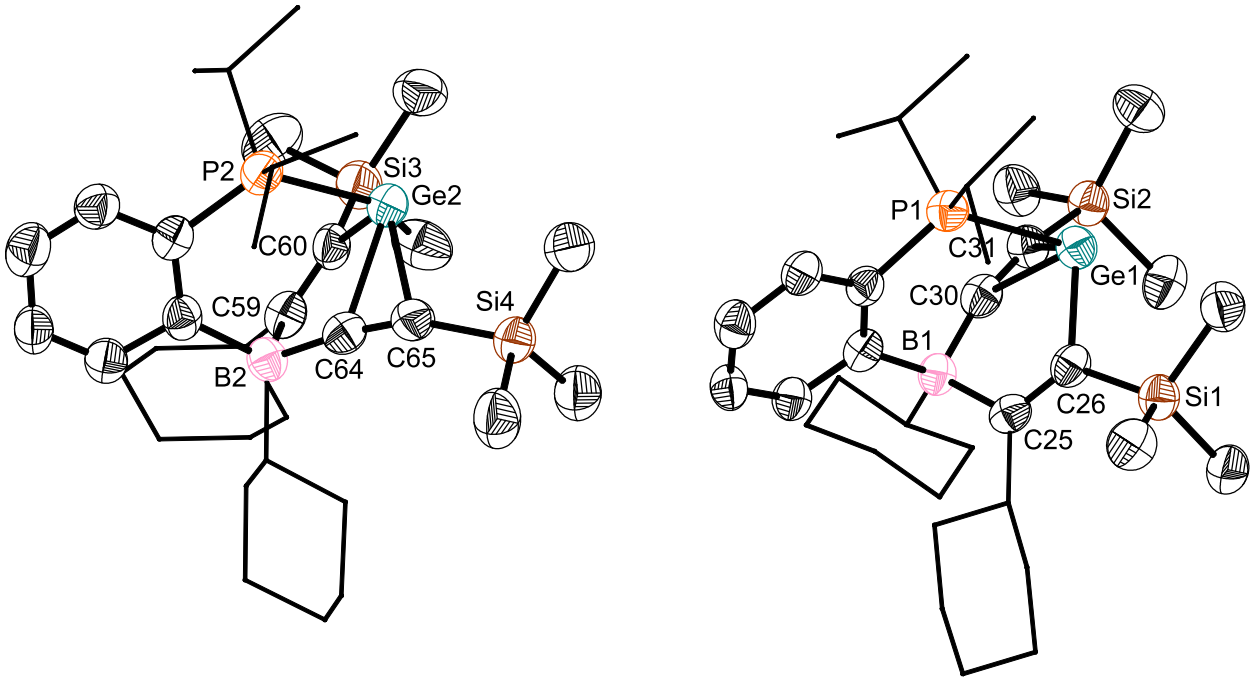

Fig. S23. The asymmetric unit in the crystal of **6**, showing the molecular structures for both enantiomers present. Thermal ellipsoids are plotted at 35 % probability, and only the major [67.2(14) %] component of the disordered trimethylsilyl group (at Si4) is shown. ^{i}Pr and Cy groups are shown in wireframe, and all H atoms have been omitted for clarity. Selected bond lengths [Å] and angles [°]: P1–Ge1 2.432(3), B1–C25 1.668(12), C25–C26 1.355(11), C26–Ge1 2.019(8), B1–C30 1.602(12), C30–C31 1.259(13), Ge1–C30 2.312(8), Ge1–C31 2.248(8), P2–Ge2 2.438(3), B2–C59 1.696(14), C59–C60 1.350(11), C60–Ge2 2.021(8), B2–C64 1.582(12), C64–C65 1.234(13), Ge2–C64 2.322(8), Ge2–C65 2.255(8); P1–Ge1–C31 95.5(3), P1–Ge1–C26 94.5(3), C26–Ge1–C31 104.4(3), C30–Ge1–C31 32.0(3), P2–Ge2–C65 94.7(3), P2–Ge2–C60, 95.2(3), C60–Ge2–C65 103.7(3), C64–Ge2–C65 31.2(3).

3. Thermogravimetric analysis

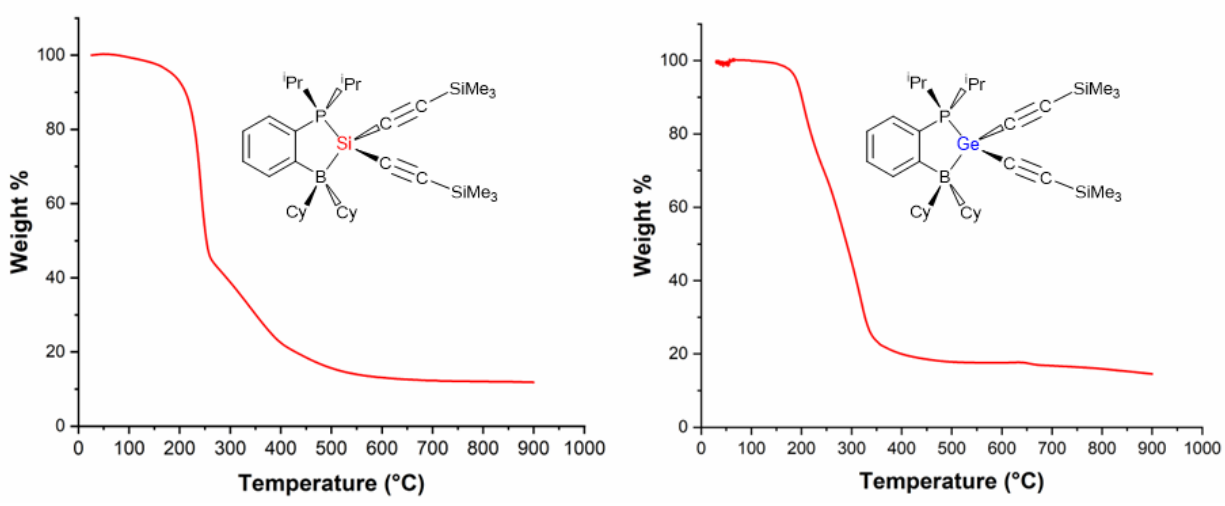

Fig. S24. TGA curve for (A) PB{Si(C≡CSiMe$_3$)$_2$} (**3**) which shows the onset of weight loss (99.5 %) is 97 °C and the residual mass (at 900 °C) is 11.8 %, and (B) PB{Ge(C≡CSiMe$_3$)$_2$} (**4**) which shows the onset of weight loss (99.5 %) is 136 °C and the residual mass (at 900 °C) is 14 %.

4. Fourier transform-infrared (FT-IR) spectra

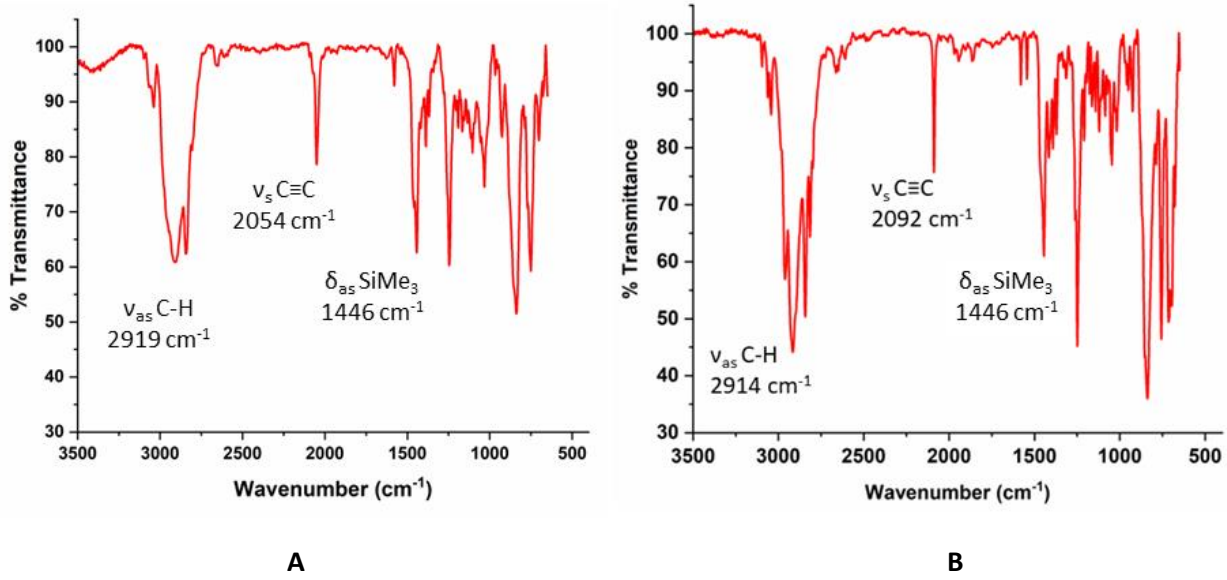

Fig. S25. FT-IR spectrum for (A) PB{Si(C≡CSiMe$_3$)$_2$} (**3**) and (B) PB{Ge(C≡CSiMe$_3$)$_2$} (**4**). υ - stretching mode; δ - deformation; as – asymmetric; s – symmetric. Assignments were made via comparison with previously reported values.

5. Density functional theory (DFT) computations

Using Gaussian16,[S5] structure geometries were optimized in the gas phase with the M06-2X functional[S6] and the cc-pVTZ basis set.[S7] All computations used Gaussian's ultrafine grid. Frequency analyses were performed to confirm the absence of imaginary frequencies for optimized geometries, and one imaginary frequency for transition states. Optimized geometries and orbitals were visualized with Avogadro;[S8] MOs and NBOs are plotted with isosurface values of +/– 0.02 and +/– 0.04, respectively. Natural bond orbital (NBO) analyses were preformed at the same level of theory as the geometry optimizations/frequency analyses, using the NBO 6.0 program.[S9] Atoms in molecules (AIM)[S10] analysis was performed using the Multiwfn 3.8 program[S11] and imaged using VMD.[S12]

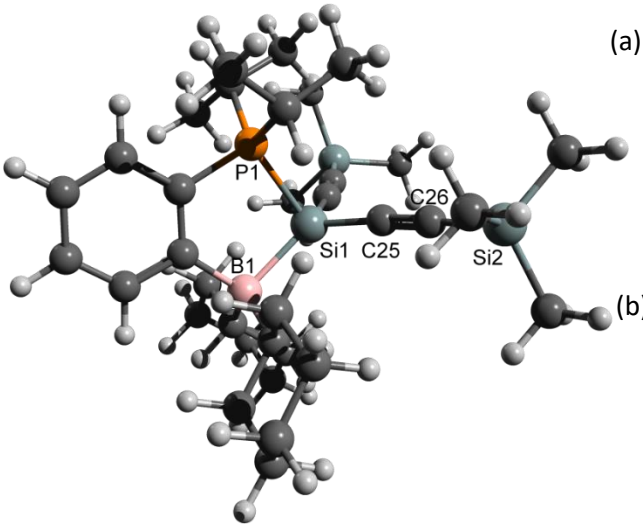

(a)

Bond	Calculated	Experimental
P1–Si1	2.317	2.3050(6)
B1–Si1	2.083	2.0706(16)
Si1–C25	1.842	1.8451(15)
C25–C26	1.214	1.202(2)
C26–Si2	1.848	1.8523(17)

(b)

Bond	WBI	Atom	Q_{NPA}
P1–Si1	0.74	P1	1.09
B1–Si1	0.86	B1	0.19
Si1–C25	0.81	Si1	1.18
C25–C26	2.87	Si2	1.67
C26–Si2	0.77	C25	–0.47
-	-	C26	–0.46

Table S5. Optimized gas-phase geometry of PB{Si(C≡CSiMe$_3$)$_2$} (**3**) (M06-2X/cc-pVTZ) with (*a*) calculated and experimental bond lengths [Å], and (*b*) Wiberg bond indices (WBI) and natural charges (Q_{NPA}).

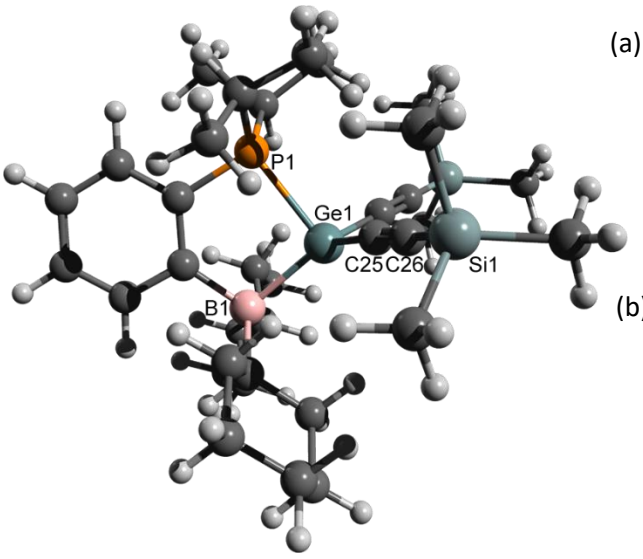

(a)

Bond	Calculated	Experimental
P1–Ge1	2.404	2.3695(8)
B1–Ge1	2.163	2.157(3)
Ge1–C25	1.933	1.928(3)
C25–C26	1.214	1.205(4)
C26–Si1	1.848	1.841(3)

(b)

Bond	WBI	Atom	Q_{NPA}
P1–Ge1	0.71	P1	1.06
B1–Ge1	0.85	B1	0.28
Ge1–C25	0.78	Ge1	1.20
C25–C26	2.88	Si1	1.67
C26–Si2	0.77	C25	–0.51
-	-	C26	–0.49

Table S6. Optimized gas-phase geometry of PB{Ge(C≡CSiMe$_3$)$_2$} (**4**) (M06-2X/cc-pVTZ) with (*a*) calculated and experimental bond lengths [Å], and (b) Wiberg bond indices (WBI) and natural charges (Q_{NPA}).

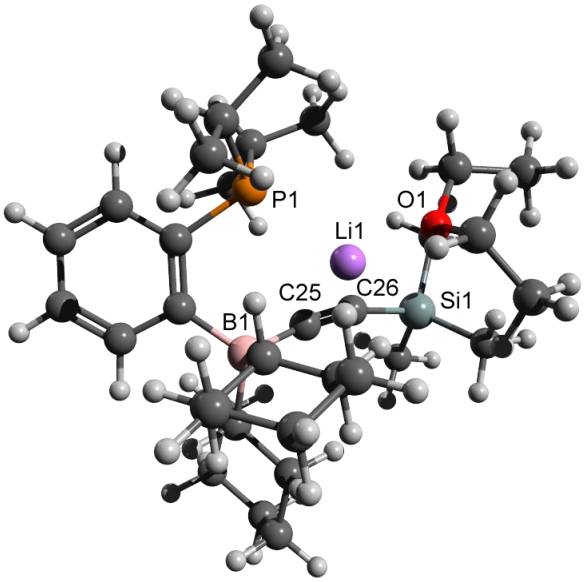

(a)

Bond	Calculated	Experimental
P1–Li1	2.498	2.492(7)
Li1–O1	1.918	1.881(8)
B1–C25	1.604	1.622(6)
C25–C26	1.223	1.205(6)
C25–Li1	2.134	2.226(8)
C26–Li1	2.310	2.261(9)

(b)

Bond	WBI	Atom	Q_{NPA}
B1–C25	0.90	P1	0.75
C25–C26	2.80	B1	0.29
-	-	Li1	0.83
-	-	O1	–0.65
-	-	C25	–0.12
-	-	C26	–0.70

Table S7. Optimized gas-phase geometry of [^{i}Pr$_2$P(C$_6$H$_4$)BCy$_2$(C≡CSiMe$_3$)Li(OEt$_2$)] (**5**) (M06-2X/cc-pVTZ) with (*a*) calculated and experimental bond lengths [Å], and (*b*) Wiberg bond indices (WBI) and natural charges (Q_{NPA}).

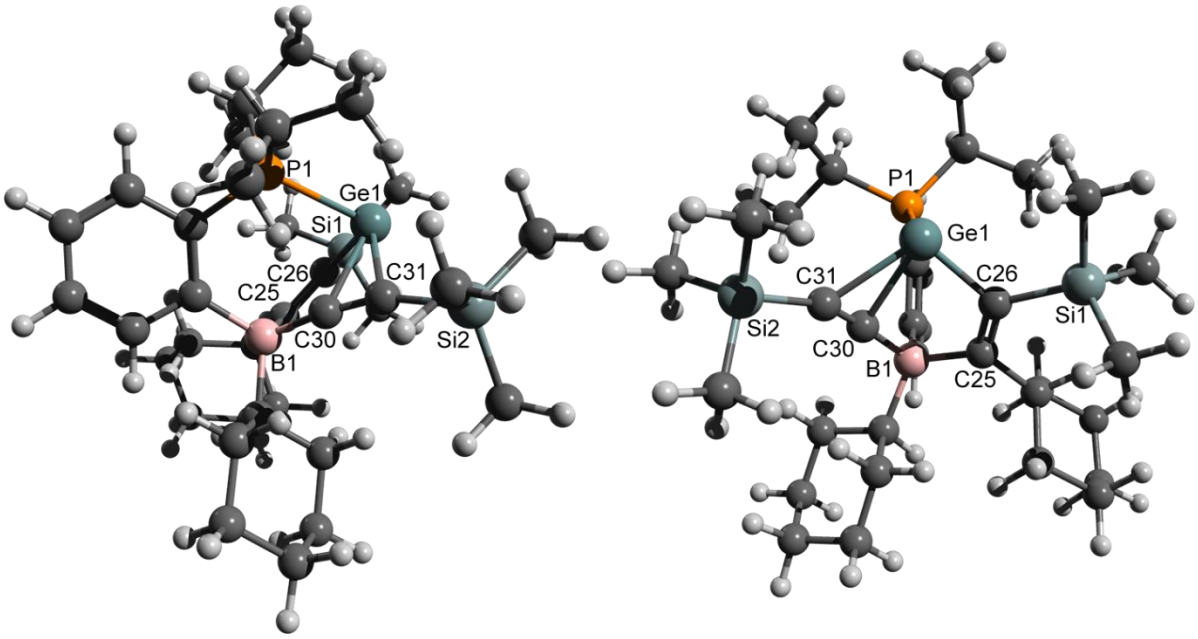

(a)

Bond	Calculated	Experimental
P1–Ge1	2.480	2.438(3)
Ge1–C26	2.006	2.021(8)
C25–C26	1.357	1.350(11)
B1–C25	1.658	1.696(14)
B1–C30	1.599	1.582(12)
C30–C31	1.236	1.234(13)
Ge1–C30	2.341	2.322(8)
Ge1–C31	2.285	2.255(8)

(b)

Bond	WBI	Atom	Q_{NPA}
P1–Ge1	0.62	P1	1.02
Ge1–C26	0.71	B1	0.24
C25–C26	1.86	Ge1	0.89
B1–C25	0.84	C25	–1.06
B1–C30	0.88	C26	–0.07
C30–C31	2.55	C30	–0.08
Ge1–C30	0.26	C31	–0.73
Ge1–C31	0.27	Si1	1.76
-	-	Si2	1.73

Table S8. Optimized gas-phase geometry of **6** (M06-2X/cc-pVTZ) with (*a*) calculated and experimental bond lengths [Å], and (*b*) Wiberg bond indices (WBI) and natural charges (Q_{NPA}).

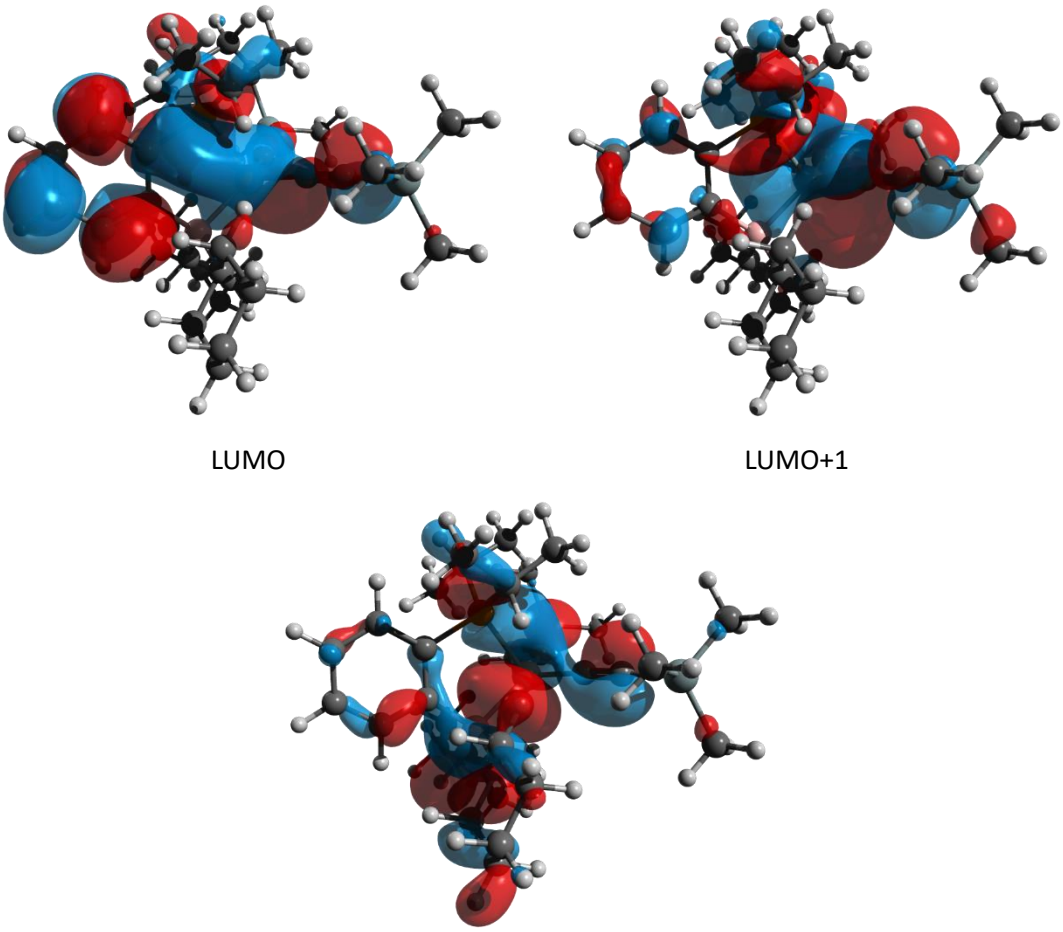

Fig. S26. Computed HOMO (–6.99 eV), LUMO (–0.30 eV), and LUMO+1 (–0.01 eV) of PB{Si(C≡CSiMe$_3$)$_2$} (**3**) (gas phase, M06-2X/cc-pVTZ).

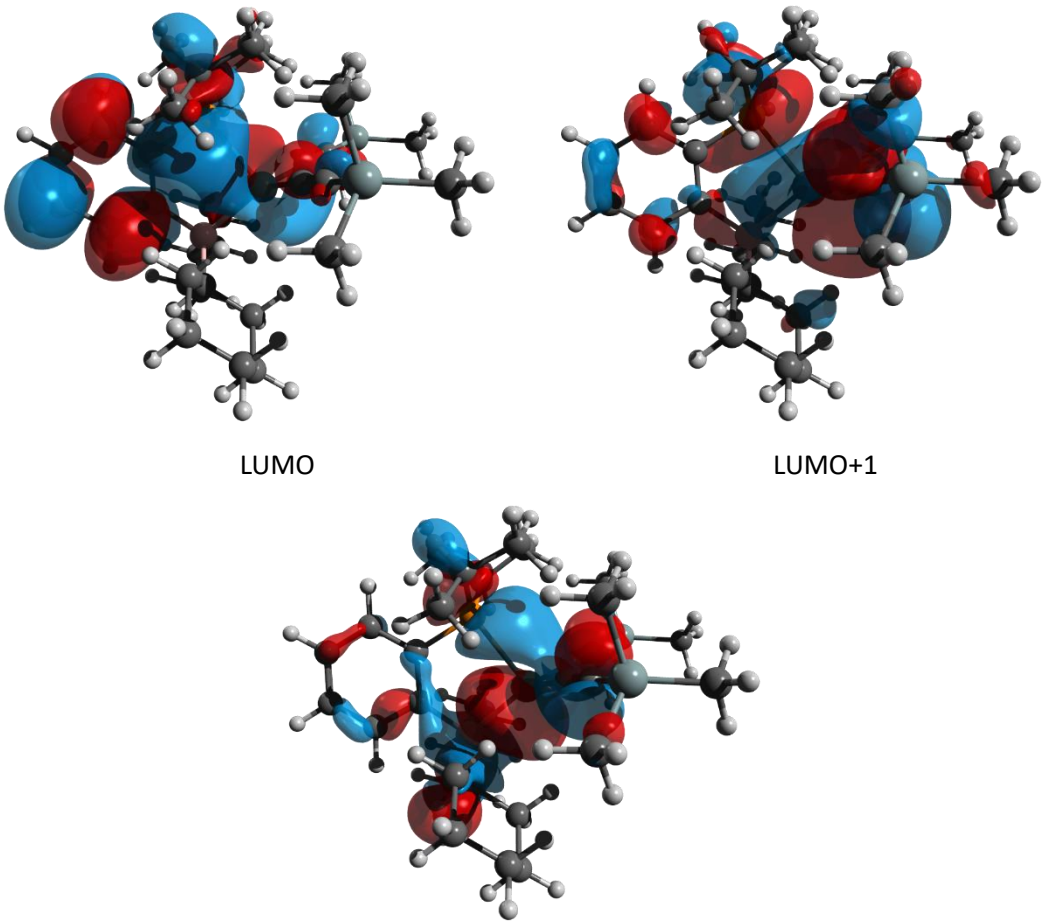

Fig. S27. Computed HOMO (–7.06 eV), LUMO (–0.24 eV), and LUMO+1 (0.04 eV) of PB{Ge(C≡CSiMe$_3$)$_2$} (**4**) (gas phase, M06-2X/cc-pVTZ).

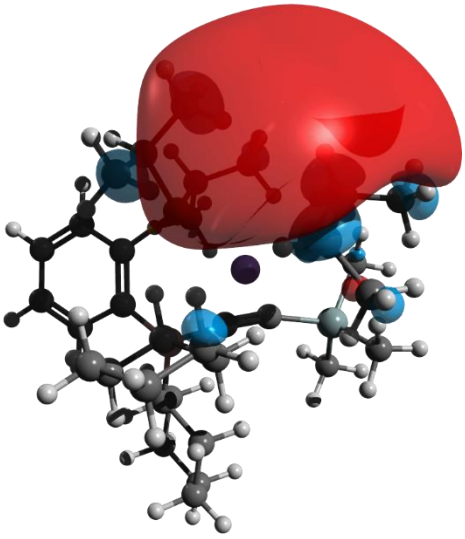

LUMO

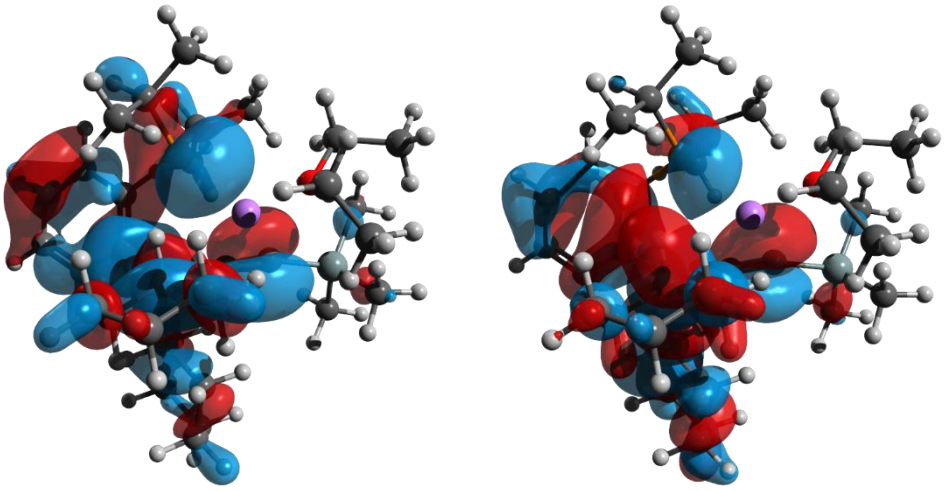

HOMO–1 HOMO

Fig. S28. Computed HOMO–1 (–7.30 eV), HOMO (–7.12 eV), and LUMO (–0.03 eV) of [^{i}Pr$_2$P(C$_6$H$_4$)BCy$_2$(C≡CSiMe$_3$)Li(OEt$_2$)] (**5**) (gas phase, M06-2X/cc-pVTZ).

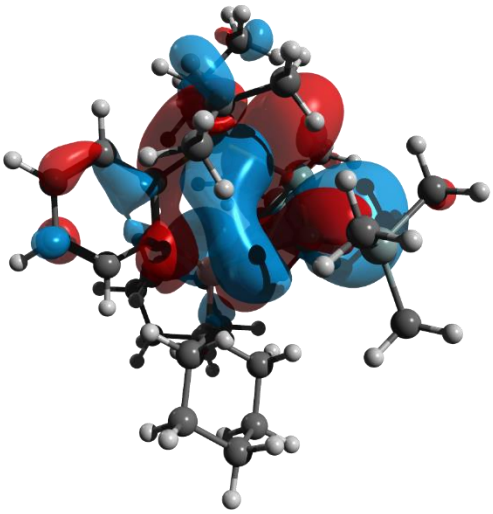

LUMO

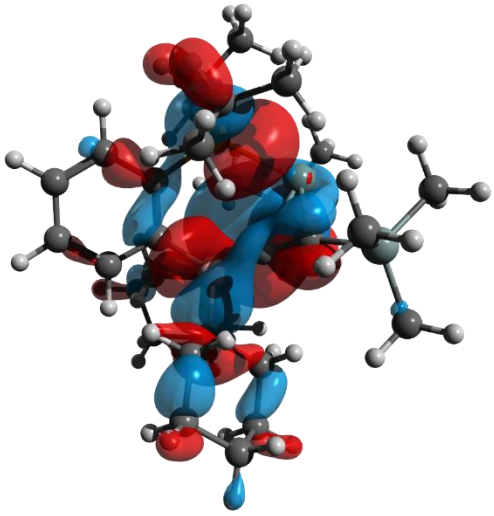

HOMO–1

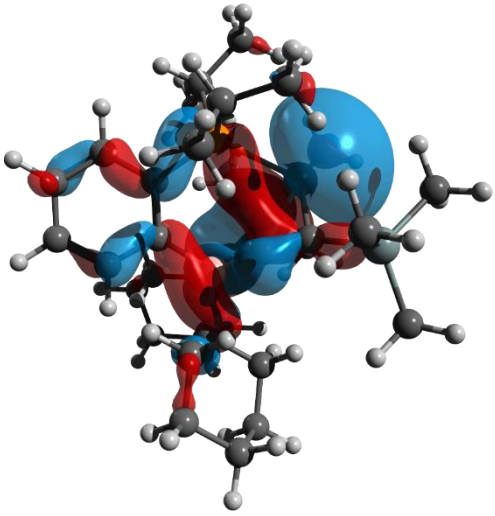

HOMO

Fig. S29. Computed HOMO–1 (–7.26 eV), HOMO (–6.51 eV), and LUMO (–0.30 eV) of **6** (gas phase, M06-2X/cc-pVTZ).

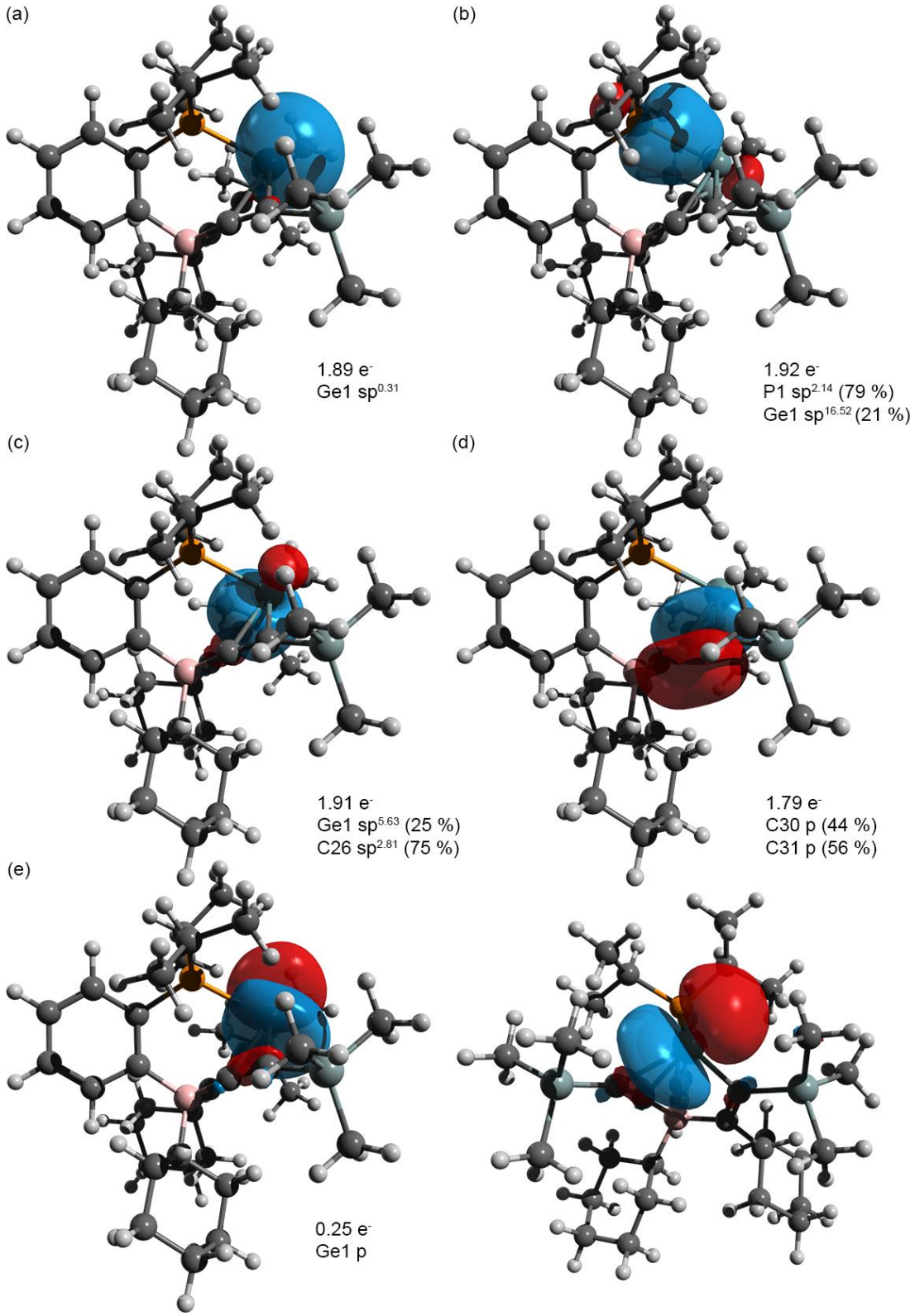

Fig. S30. Selected computed NBOs, along with their occupancies and compositions, of **6** (gas phase, M06-2X/cc-pVTZ) showing (*a*) the LP on Ge1, (*b*) the P1–Ge1 σ-bond, (*c*) the Ge1–C26 σ-bond, (*d*) the C30–C31 π-bond, and (*e*) two views of the empty p-orbital at Ge1.

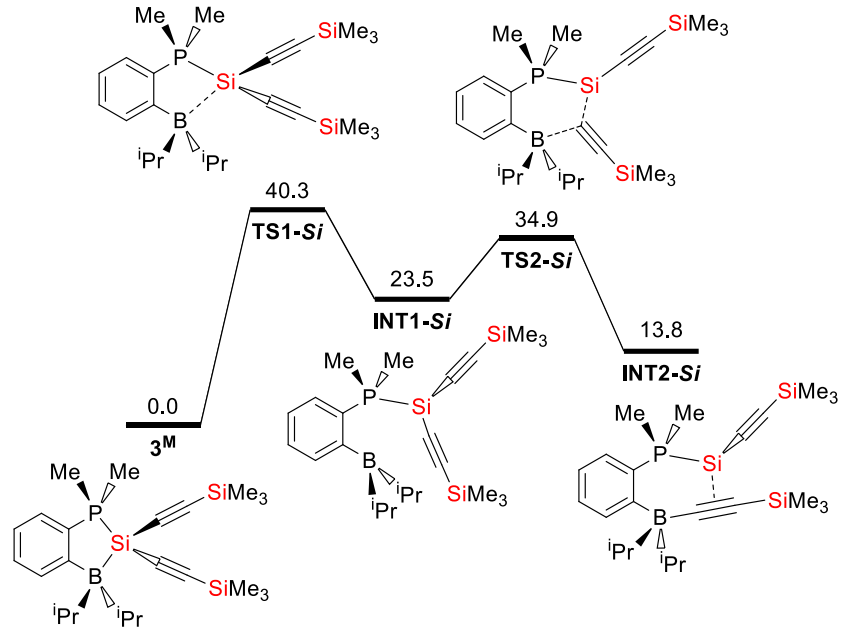

Fig. S31. Computed (gas phase, M06-2X/cc-pVTZ) free energy pathway for the cleavage of the B–Si bond in the model compound **3**^{M} and subsequent alkynyl transfer from Si to B. Free energies are listed in kcal mol^{-1}.

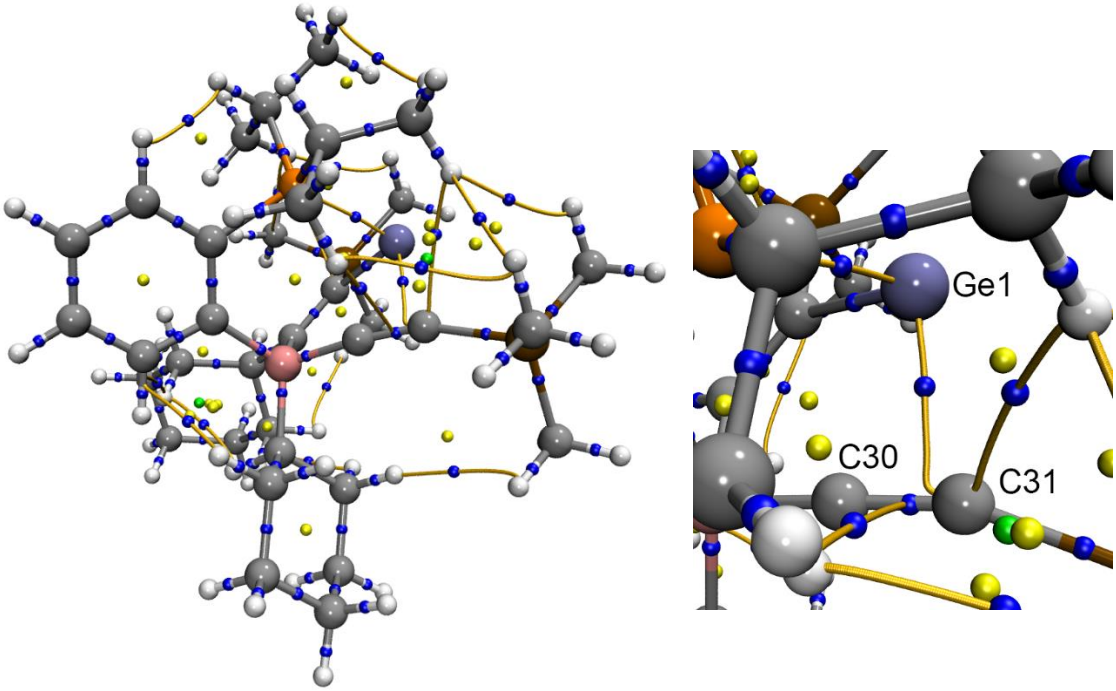

Fig. S32. Atoms in molecules (AIM) critical points and paths (yellow lines) for **6** (M06-2X/cc-pVTZ). Bond critical points (bcps) are in blue, ring critical points (rcps) in yellow, and cage critical points in green. Note the absence of an rcp for the Ge1–C30–C31 atoms.

Table S9. Real space bonding indicators derived from AIM analysis of **6** (M06-2X/cc-pVTZ).

Bond	ρ(r) [e Å^{-3}]	$\nabla^2\rho(r)$ [e Å^{-5}]	ε	η
Ge1–C31	0.41	1.90	1.09	0.35
C30–C31	2.82	–35.10	0.08	7.14
P1–Ge1	0.46	0.55	0.19	0.46

Here, ρ(r) and $\nabla^2\rho(r)$ are the electron density and its Laplacian at the bcp; ε is the ellipticity; and η is the ratio of the smallest to largest eigenvalue in the Hessian matrix of ρ(r).

The low ρ(r) values at the Ge1–C31 and P1–Ge1 bcps, along with their positive Laplacians, suggest the dative nature of these bonds. At the C30–C31 bcp, the large electron density and near-zero bond ellipticity are in accordance with a C30–C31 triple bond.

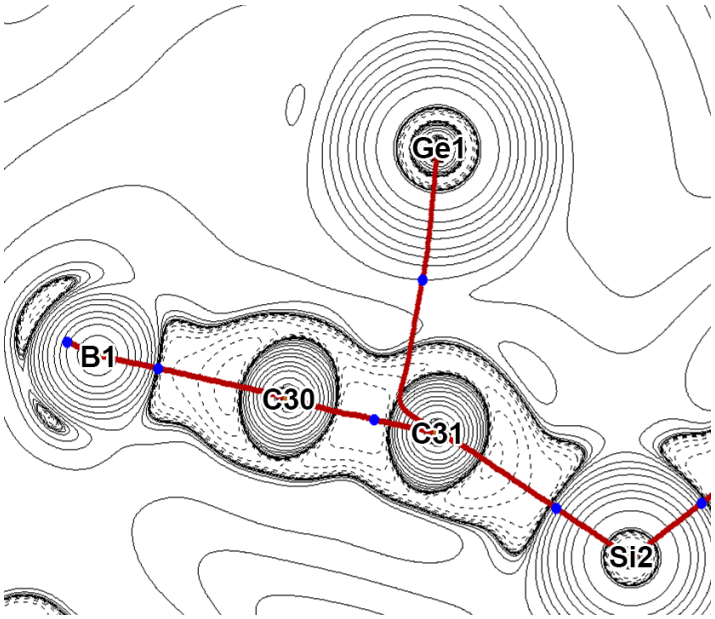

Fig. S33. 2D plot of $\nabla^2\rho(r)$ within the C30–C31–Ge1 plane of **6** (M06-2X/cc-pVTZ). Solid and dashed lines represent areas of local charge depletion and concentration, respectively. Bond critical points are represented by blue dots, and the bond paths are in red.

6. References

S1 R. H. Blessing, *Acta Cryst*. *A*, 1995, **51**, 33–38.

S2 G. M. Sheldrick, *Acta Cryst. C*, 2015, **71**, 3–8.

S3 O. V. Dolomanov, L. J. Bourhis, R. J. Gildea, J. A. K. Howard and H. Puschmann, *J. Appl. Cryst.,* 2009, **42**, 339–341.

S4 H. Putz and K. Brandenburg, Diamond - Crystal and Molecular Structure Visualization, Crystal Impact, Bonn, Germany, (http://www.crystalimpact.com/diamond).

S5 M. J. Frisch, G. W. Trucks, H. B. Schlegel, G. E. Scuseria, M. A. Robb, J. R. Cheeseman, G. Scalmani, V. Barone, G. A. Petersson, H. Nakatsuji, X. Li, M. Caricato, A. V. Marenich, J. Bloino, B. G. Janesko, R. Gomperts, B. Mennucci, H. P. Hratchian, J. V. Ortiz, A. F. Izmaylov, J. L. Sonnenberg, D. Williams-Young, F. Ding, F. Lipparini, F. Egidi, J. Goings, B. Peng, A. Petrone, T. Henderson, D. Ranasinghe, V. G. Zakrzewski, J. Gao, N. Rega, G. Zheng, W. Liang, M. Hada, M. Ehara, K. Toyota, R. Fukuda, J. Hasegawa, M. Ishida, T. Nakajima, Y. Honda, O. Kitao, H. Nakai, T. Vreven, K. Throssell, J. A. Montgomery Jr., J. E. Peralta, F. Ogliaro, M. J. Bearpark, J. J. Heyd, E. N. Brothers, K. N. Kudin, V. N. Staroverov, T. A. Keith, R. Kobayashi, J. Normand, K. Raghavachari, A. P. Rendell, J. C. Burant, S. S. Iyengar, J. Tomasi, M. Cossi, J. M. Millam, M. Klene, C. Adamo, R. Cammi, J. W. Ochterski, R. L. Martin, K. Morokuma, O. Farkas, J. B. Foresman and D. J. Fox, Gaussian 16 (version Revision B.01) Gaussian, Inc., Wallingford, CT 2016.

S6 Y. Zhao and D. G. Truhlar, *Theo. Chem. Acc.*, 2008, **120**, 215–241.

S7 T. H. Dunning, *J. Chem. Phys.*, 1989, **90**, 1007–1023.

S8 M. D. Hanwell, D. E. Curtis, D. C. Lonie, T. Vandermeersch, E. Zurek and G. R. Hutchison, *J. Cheminf.*, 2012, **4**, 17.

S9 E. D. Glendening, J. K. Badenhoop, A. E. Reed, J. E. Carpenter, J. A. Bohman, C. M. Morales, C. R. Landis and F. Weinhold, NBO 6.0, Theoretical Chemistry Institute, University of Wisconsin, Madison, WI 2013.

S10 R. W. F. Bader, *Chem. Rev.*, 1991, **91**, 893–928.

S11 T. Lu and F. Chen, *J. Comput. Chem.,* 2012, **33**, 580–592.

S12 W. Humphrey, A. Dalke and K. Schulten, *J. Mol. Graphics,* 1996, **14**, 33–38.